BEILSTEIN JOURNAL OF NANOTECHNOLOGY

Quantum-to-classical modeling of monolayer Ge_2Se_2 and its application in photovoltaic devices

Anup Shrivastava*[1,2], Shivani Saini[1,2], Dolly Kumari[3], Sanjai Singh[2] and Jost Adam*[1,4]

Full Research Paper

Open Access

Address:
[1]Computational Materials and Photonics (CMP), Department of Electrical Engineering and Computer Science, University of Kassel, Kassel, Germany, [2]Computational Nano-Material Research Lab (CNMRL), Indian Institute of Information Technology, Allahabad, Uttar Pradesh, India, [3]Department of Electrical Engineering, Indian Institute of Technology, Patna, India and [4]Center for Interdisciplinary Nanostructure Science and Technology (CINSaT), University of Kassel, Kassel, Germany

Email:
Anup Shrivastava* - anup@uni-kassel.de;
Jost Adam* - jost.adam@uni-kassel.de

* Corresponding author

Keywords:
2D materials; density functional theory; hole transport layer; optical properties; solar cells

Beilstein J. Nanotechnol. **2024,** *15,* 1153–1169.
https://doi.org/10.3762/bjnano.15.94

Received: 30 April 2024
Accepted: 21 August 2024
Published: 11 September 2024

This article is part of the thematic issue "Smart nanomaterials in electronics and photonics".

Associate Editor: M. H. Kim

© 2024 Shrivastava et al.; licensee Beilstein-Institut.
License and terms: see end of document.

Abstract

Since the discovery of graphene in 2004, the unique properties of two-dimensional materials have sparked intense research interest regarding their use as alternative materials in various photonic applications. Transition metal dichalcogenide monolayers have been proposed as transport layers in photovoltaic cells, but the promising characteristics of group IV–VI dichalcogenides are yet to be thoroughly investigated. This manuscript reports on monolayer Ge_2Se_2 (a group IV–VI dichalcogenide), its optoelectronic behavior, and its potential application in photovoltaics. When employed as a hole transport layer, the material fosters an astonishing device performance. We use ab initio modeling for the material prediction, while classical drift–diffusion drives the device simulations. Hybrid functionals calculate electronic and optical properties to maintain high accuracy. The structural stability has been verified using phonon spectra. The *E*–*k* dispersion reveals the investigated material's key electronic properties. The calculations reveal a direct bandgap of 1.12 eV for monolayer Ge_2Se_2. We further extract critical optical parameters using the Kubo–Greenwood formalism and Kramers–Kronig relations. A significantly large absorption coefficient and a high dielectric constant inspired the design of a monolayer Ge_2Se_2-based solar cell, exhibiting a high open circuit voltage of V_{oc} = 1.11 V, a fill factor of 87.66%, and more than 28% power conversion efficiency at room temperature. Our findings advocate monolayer Ge_2Se_2 for various optoelectronic devices, including next-generation solar cells. The hybrid quantum-to-macroscopic methodology presented here applies to broader classes of 2D and 3D materials and structures, showing a path to the computational design of future photovoltaic materials.

Introduction

Reducing fossil fuels and their harmful environmental impact requires improvements in green, sustainable energy sources. Among the various sources of green energy generation, solar energy has been identified as the most promising and expedient because it has the potential to address the current energy demand without making a hazardous impact on the environment [1,2]. Henceforth, researchers have made continuous efforts to design efficient and robust PV devices and solar cells. The systematic study of various solar cells in the last few decades has led to many successful breakthroughs in terms of the stability, efficiency, and cost of PV technology. In the past few decades, perovskite solar cells (PSCs) have emerged as a groundbreaking technology in the field of renewable energy because of their remarkable efficiency and relatively low manufacturing cost [3,4]. These solar cells are based on perovskite-structured compounds, which have demonstrated excellent light absorption, charge-carrier mobilities, and tunable bandgaps [5].

Despite the rapid advancements in PSC technology, some critical issues, such as long-term instability, poor device scalability, and the use of toxic compounds, have yet to be resolved [6]. Recent advancements have seen the integration of two-dimensional (2D) materials with PSCs, opening new avenues for enhancing their performance and addressing current challenges with the PSCs [7,8]. Integrating 2D materials in PSCs can improve their performance. The 2D materials can provide protective layers that work like a shield to the perovskite materials to protect them from environmental degradation caused by moisture and oxygen and provide better device scalability to the PSCs, which makes large-scale production more feasible [9]. Also, the mechanical robustness and flexibility of the 2D materials will give extra room to design the PSCs for a wide range of applications areas [10]. The high carrier mobility and enhanced optoelectronic characteristics can improve the device performance of conventional PSCs [11], and the use of non-toxic 2D materials can improve the performance of PSCs without health risks.

Many researchers recently proposed an ultrathin transport layer-based solar cell as the most expedient photo device for sunlight harvesting. The general scheme of a solar cell comprises various layers including the active/absorber layers, the electron transport layer (ETL) and the hole transport layer (HTL) [12,13]. Both HTL and ETL play a crucial role in achieving a high performance of PV devices. The most common HTL material is spiro-OMeTAD, but it is very expensive [14]. Furthermore, a large number of materials have been reported as ETLs/HTL materials, such as carbon [15], copper iodide [16], $CuSbS_2$, NiO, CuSCN [17], ZnO, and CdS [18]. These materials promote efficient extraction of charge carriers and suppress recombination between the perovskite film and the electrodes. But in all these cases, the transport layer thicknesses are taken as sufficiently high. During the last few decades, researchers claimed that ETLs/HTLs of two-dimensional materials could achieve high power conversion efficiency (PCE) and optimum device performance [18,19]. The key features of the 2D materials, rendering them viable for PV applications were discussed in [20].

Because of the advantages of 2D materials, tremendous efforts have been made to invent highly stable and efficient solar cells based on 2D materials. A number of remarkable works have been recently reported using numerous 2D materials, including MXene's, transition-metal dichalcogenides (TMDCs) and van der Waals structures [21]. Among the various sets of 2D materials, TMDCs (with the general formula of MX_2, where M is a transition metal and X is a chalcogen) attract the broad attention of the research community regarding their extensive applications in photodevices. This is mainly because of the exceptional optoelectronic behavior of the TMDCs, especially the layer-dependent bandgap and the high absorption of incident sunlight [22-25]. Motivated by this, various TMDCs, including MoS_2, WS_2, WSe_2, and TiS_2, have been used in PSCs, either as HTL or as ETL. Yin et al. [26] reported a PCE of approximately 17.3% with TiS_2 nanosheets suspended in isopropanol alcohol in a PSC. 2D sheets of SnS_2 have been proposed by Zhao et al. [27] as a prospective ETL for PSCs. It achieved a maximum PCE of around 20%. Similarly, other PSCs using different 2D layers of TMDCs have been reported (summarized below in Table 3). Despite the pervasive use of TMDC-based 2D materials in solar cells, their device performance still leaves room for improvement.

Recently, a new class of dichalcogenides (group IV–VI metal chalcogenides) has been successfully synthesized [28-31]. Its remarkable features, such as low cost, abundance, environmental friendliness, and many interesting physical properties, indicate a broad range of possible applications in sustainable electronics and photonics [32]. Notably, a high absorption coefficient has been reported in [33] for an SnS monolayer across the direct absorption edge at 1.3–1.5 eV, rendering it potentially applicable in solar cells and photodetectors. Similarly, Huang et al. [34] showed that a band transition (from indirect to direct) occurs in $SnSe_2$ when moving from bulk to monolayers, elucidating its application potential in optoelectronic devices. More group IV–VI dichalcogenides have been discussed in [35-40] for different applications. Although some inceptive work has been done using monolayers of metal dichalcogenides, there are still plenty of opportunities to explore. In line with the same,

we have studied the thermoelectric behavior of monolayer Ge_2Se_2 in our previous work [41].

This article aims to investigate the optoelectronic properties of the group IV–VI dichalcogenide monolayer Ge_2Se_2 using density functional theory (DFT) and to demonstrate its potential application in photovoltaic solar cells. The proposed Ge_2Se_2 monolayer exhibited excellent thermodynamic stability, higher carrier mobilities (due to the presence of valleys in the CB/VB), and good optical response (an interband transition in the visible region). Considering the proper design criteria and selecting an appropriate material for absorbers/ETL, we have designed and modeled the solar cell in a FTO–TiO_2–$CsSn_{0.5}Ge_{0.5}I_3$–Ge_2Se_2–Ag configuration, which outperforms, in terms of their key parameters, other reported works in the literature. The proposed solar cell configuration is environmentally friendly (absence of toxic materials), of low cost, and highly efficient. The computational methodology followed here is depicted in Figure 1, and we provide detailed corresponding instructions and references in the Methods section.

Results and Discussion

The computational approach can be better explained by separating it into two subsections, namely (a) material simulation using DFT and (b) device simulation using a macroscopic approach, which will be discussed in section Computational Methods.

Structural and stability analysis

The schematic atomistic model for monolayer Ge_2Se_2 is shown in Figure 2. For better understanding, a side view of monolayer Ge_2Se_2 with the corresponding lattice parameters is given in Figure 2a, and the top view of the supercell of the order 4 × 4 is shown in Figure 2b. From Figure 2a, we can observe that the unit cell of monolayer Ge_2Se_2 consists of four atoms (two for each Ge and Se). More precisely, we can observe two sublayers corresponding to a crystallogen (Ge) and a chalcogen (Se), which are designate as top and bottom moieties. From Figure 2, we can also notice that the structure of monolayer Ge_2Se_2 is identical to the puckered phosphorene (simple orthorhombic structure) with space group symmetry of $Pmn2_1$ (C_{2v}^7) in 2D space.

The geometry-optimized lattice parameters a and b are found to be 4.13 and 3.99 Å, respectively. The bond lengths between consecutive crystallogen and chalcogen (Ge–Se) are 2.59 and 2.67 Å in the horizontal and vertical directions, respectively. All optimized structural parameters excellently match with previously reported values [41,42]. In addition to the lattice parameters for the monolayer Ge_2Se_2, we have optimized the vacuum slab in a normal direction to avoid interlayer interactions. The

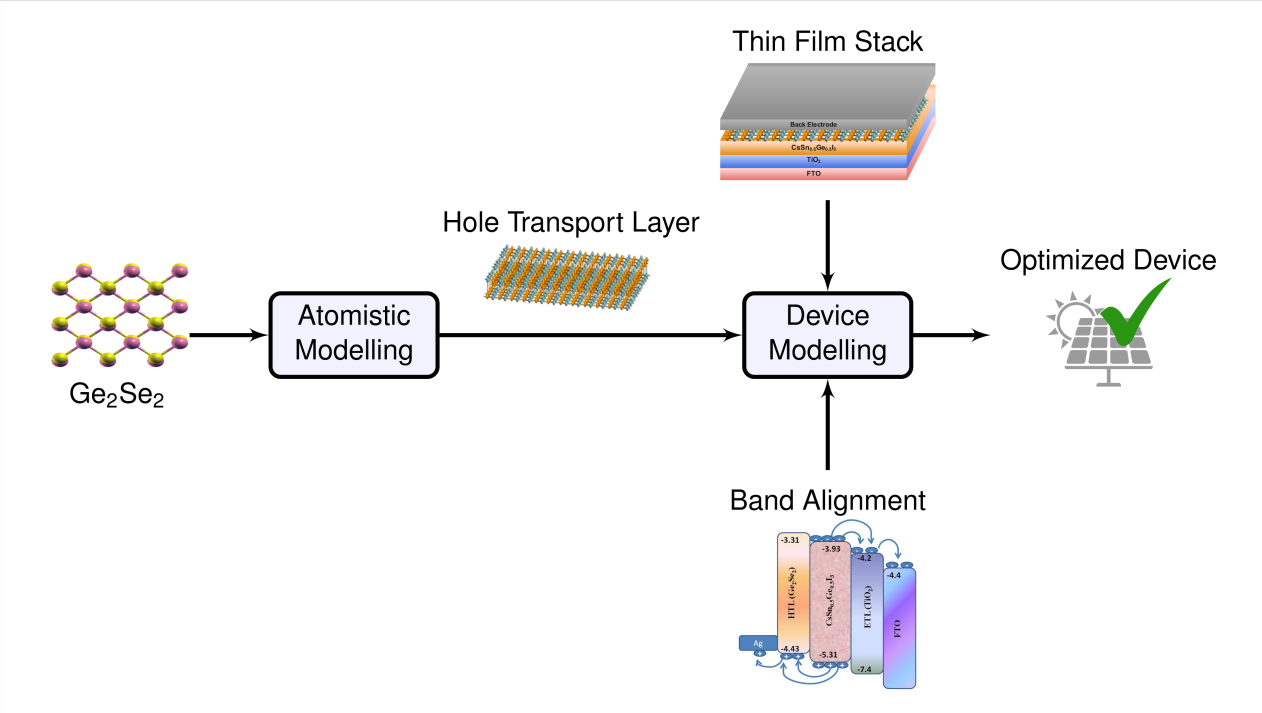

Figure 1: Optoelectronic property investigation of a group IV–VI dichalcogenide monolayer (Ge_2Se_2), and its application potential for hole transport layers in Ge_2Se_2/$CsSnGeI_3$/TiO_2-based solar cells. Our computational approach combines density functional theory and atomistic modeling with (macroscopic) device modeling to obtain an otimized device performance.

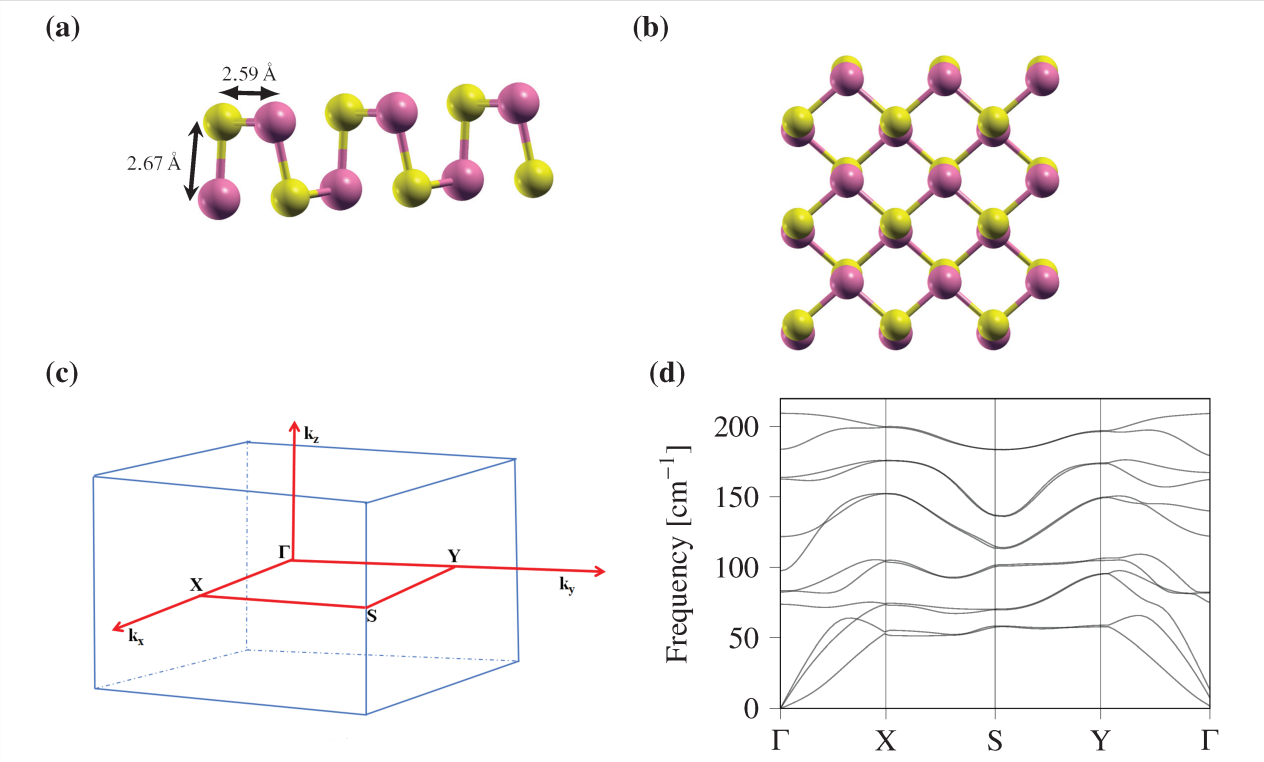

Figure 2: Geometry and stability of Ge_2Se_2 monolayers. (a) Side view with the corresponding structural parameters and (b) top view. The exhibited structure is a simple orthorhombic structure with space group symmetry of *Pmn*2$_1$ (C_{2v}^7) in 2D space. (c) Brillouin zone, where the Γ-X-S-Y-Γ path is used to plot the phonon spectra, and (d) phonon dispersion, confirming the structure's dynamical stability (Figure 2a,b were redrawn from [41], Figure 2d was re-plotted from [41]).

optimized vacuum level was found to be 23 Å. Furthermore, to test the stability of the crystal structure, we have computed the phonon band dispersion for monolayer Ge_2Se_2 within the first Brillouin zone (Figure 2c). The calculated phonon spectra along the high symmetry path Γ-X-S-Y-Γ in the first Brillouin zone are shown in Figure 2d.

The phonon spectrum for monolayer Ge_2Se_2 has twelve vibrational modes, of which three are acoustical (low-frequency) modes (transverse acoustic, longitudinal acoustic, and flexural acoustic). The remaining nine (high-frequency) modes correspond to optical modes. The flexural acoustic mode is an out-of-plane transverse acoustic mode, similar to those in other two-dimensional materials such as graphene, phosphorene, and stanene, demonstrating a quadratic nature near the Γ point [43-45]. Figure 2d clearly depicts that all phonon bands throughout the spectrum have non-imaginary frequency, further confirming the investigated structure's dynamic stability.

Electronic and transport properties

The electronic properties of materials play a crucial role in predicting the material behavior and transport parameters and, hence, its prospective applications. We investigated the electronic properties of monolayer Ge_2Se_2 using its electronic band structure and density of states, as shown in Figure 3. To maintain a high degree of accuracy, we calculated the band structure using the HSE06 functional, and the band dispersion along the high symmetry paths Γ-X-S-Y-Γ in the first Brillouin zone, as shown in Figure 3.

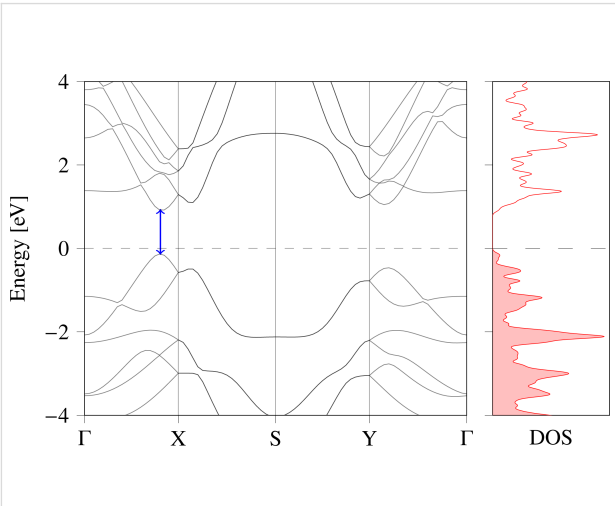

Figure 3: The electronic band structure of monolayer Ge_2Se_2, revealing a direct bandgap of 1.12 eV, and the corresponding density of states (The electronic band structure was re-plotted from [41]).

Figure 3 depicts that the monolayer Ge_2Se_2 is a direct-bandgap semiconductor with a bandgap of the order of 1.12 eV. Valence band maximum (VBM) and conduction band minimum (CBM) are located along the Γ-X path. The computed bandgap value and its dispersion nature are consistent with earlier reported works [41,42,46,47]. The optimum bandgap value and its CBM/VBM positions make it suitable for photovoltaic applications and provide a guideline for selecting the absorber layers in the solar cells. Notably, multivalley and flat bands are present in the energy band structure. The formation of multiple valleys provides extra carrier pockets for transportation, further increasing carrier mobility. Also, the larger valley degeneracy will increase the density of states (DOS) effective mass without influencing the carrier mobility. We have also calculated the total DOS to understand and justify the band structure calculation. Figure 3 shows that the calculated DOS is consistent with the electronic band structure and the bandgap values, further validating the results.

Other properties that will be useful in the simulation of solar cells, such as the effective mass of charge carriers (electrons/holes), conduction/valence band density of states, electron/hole mobility, electron affinity, and work function can be derived from the initial band energy calculation.

We calculated the effective masses of electrons and holes as $m_e^* = 0.167m_e$ and $m_h^* = 0.1768m_e$, respectively, which are very close to the values ($m_e^* = 0.17m_e$, and $m_h^* = 0.17328m_e$) reported in the literature [46,47]. With that, we estimated the effective DOS values in the CB and the VB to be 0.1732×10^{19} /cm^3 and 0.1887×10^{19} /cm^3, respectively. The electron and hole thermal velocities for monolayer Ge_2Se_2 were estimated as 9.43×10^5 m/s and 2.668×10^5 m/s, respectively. The predicted charge carrier mobilities were found to be 187.003 cm^2/(V·s) and 300.451 cm^2/(V·s) for holes and electrons, respectively. The high carrier mobility further suggests a potential application as a transport layer in solar cells as well as in the channel materials of FETs. It is important to note that although in the case of solar cells, the transmission of charge carriers takes place in the out-of-plane direction, which is usually considered to be low compared to the in-plane mobility (especially in the bulk materials), the charge carriers still move quickly across the thin HTL because of the ultrathin layer and the strong electric field gradient from the active layer to the electrode. Finally, higher in-plane mobility of the monolayers can compensate the potential limitations of out-of-pane mobility for its prospective uses in solar cells, V-FETs, TFETs, and memristors [48].

In the present calculation, we have calculated the average planar electrostatic potential along the plane as demonstrated in Figure 4. The figure depicts the vacuum energy level and the positions of HOMO and LUMO. The calculated work function and electron affinity for monolayer Ge_2Se_2 are about 3.313 and 3.873 eV, respectively, which are comparable with previously reported values of 3.39 eV and 3.9 eV [46,47].

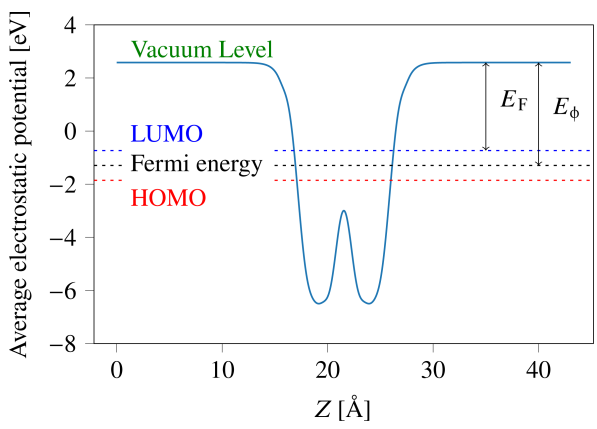

Figure 4: Macroscopic potential distribution vs lattice vector in the normal direction for monolayer Ge_2Se_2. In a periodic system, the electron affinity and work function is defined as EA = $E_{Vac} - E_{LUMO}$, and $E_\phi = E_{Vac} - E_F$, where E_F is the Fermi energy level, E_ϕ is the work function, EA is the electron affinity, E_{Vac} is the vacuum energy level, and E_{LUMO} is the LUMO energy level, respectively. The calculated work function and electron affinity are about 3.313 and 3.873 eV, respectively.

A high degree of agreement for all estimated electronic parameters with earlier reported values validates the accuracy of our computation.

Optical properties

As discussed in the previous section, monolayer Ge_2Se_2 has structural stability and exhibits an optimal electronic behavior with a direct bandgap of 1.12 eV. The DFT results indicate potential applications of the investigated structure in optoelectronic devices. The optical responses at varying photonic energies and the corresponding optical wavelength are summarized in Figure 5, depicting the dielectric function ε_r (real and imaginary parts) and the refractive index n for monolayer Ge_2Se_2. The real and imaginary components of the dielectric function correspond to dispersive and absorption effects of the material. We observe that the investigated structure exhibits strongly anisotropic optical properties for which the parametric values depend on the direction of the chosen plane.

Dielectric function and absorption coefficient

The static dielectric constants (real part of ε_r at $\omega = 0$), along the in-plane (XX) and out-of-plane (ZZ) direction were calculated as 6.37 and 2.4, respectively, suggesting that monolayer Ge_2Se_2 is highly polarized along the in-plane direction.

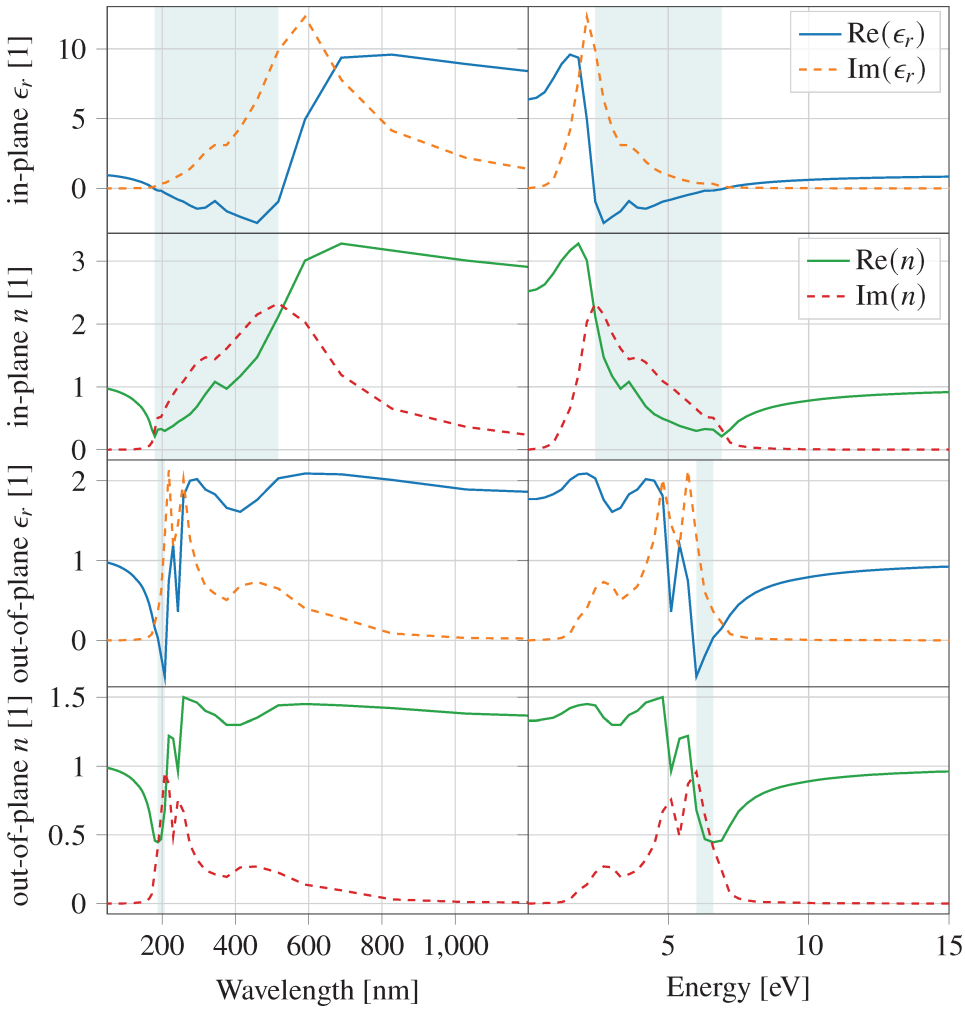

Figure 5: Optical responses of monolayer Ge_2Se_2; real (solid) and imaginary (dashed) part of the dielectric constant and refractive index vs wavelength (left) and photon energy (right), for in-plane and out-of-plane excitation relative to the sheet. The teal-colored areas mark the regions of potential metallic behavior (Re(ε_r) < 0 or, equivalently, Re(n) < Im(n)), occurring between 180 and 517 nm (2.4 and 6.9 eV) for in-plane, and between 188 and 207 nm (6.0 and 6.6 eV) for out-of-plane excitation.

The imaginary part of the dielectric function shows peaks between 2 and 3 eV, along the XX direction, which indicate an interband transition in the visible region (Figure 5). Interestingly, we can observe tracking bands (the region where the energy difference between the conduction and valence bands is approximately constant [49]) around the high-symmetry point S and between X and Y in the first Brillouin zone. Around these points, we notice a small gradient and, thus, large DOS, which further leads to higher transition possibilities.

The absorption coefficient elucidates the rate at which light intensity diminishes while entering the material. It primarily depends upon the imaginary part of the refractive index $k(\lambda) = \mathrm{Im}\{n(\lambda)\}$ and the wavelength of the incident light λ, as per $\alpha_{abs} = 4\pi k(\lambda)/\lambda$. The highest peak of the absorption coefficient lies in the visible region, which we attribute to the direct transition from VBM to CBM. The other peaks correspond to the transition from the top valence band to the conduction band in a band region of the Brillouin zone around the S point. The maximum absorption coefficient is 5×10^5 cm^{-1} along the XX direction. The highest peak for the ZZ direction is calculated as 5.8×10^5 cm^{-1}, corresponding to the UV region. We attribute this maximum to the transition from VBM to CBM, while the other peaks designate a transition from VBM to CBM around a wide range of spectra at the S point.

Refractive index and extinction coefficient

The real part of the material's refractive index defines the angle of refraction that the light undergoes while entering a medium. Higher refractive indices refer to lower refraction angles measured from the interface normal. The static refractive indices for monolayer Ge_2Se_2 in the direction parallel to the

plane (XX) and normal to the plane (ZZ) are approximately 2.5 and 1.4, respectively, as shown in Figure 5. These refractive indices could enable the use of the investigated material as an inner layer coating between the absorber and substrate/electrodes in the design of solar cells.

Device Modeling

The high carrier mobility, optimum bandgap, and suitable optical characteristics of monolayer Ge_2Se_2 as discussed in the previous section, further motivated us to design a photovoltaic solar cell using monolayered Ge_2Se_2. The easy fabrication, structural stability, and proper band alignment with the absorber material make it a promising hole transport layer (HTL) in the proposed solar cell. The proposed solar cell is a low-cost, environmentally friendly, scalable Perovskite solar cell (PSC), with Ge_2Se_2 as a HTL. The schematic of the proposed solar cell is shown in Figure 6a.

The proposed structure consists of a lead-free Perovskite layer as an absorber, titanium dioxide (TiO_2) as ETL, and Ge_2Se_2 as HTL. A 100 nm thick layer of FTO is used to encapsulate the transport and absorber layers and treated as a conductor in this simulation. Regarding an absorber material corresponding to the proposed HTL, a minimum valence band offset between these two layers has been considered as a necessary condition for achieving optimum performance. In addition to this, environmental friendliness, stability, and cost-effectiveness were also considerations to choose $CsSn_{0.5}Ge_{0.5}I_3$ as an absorber layer. After selecting the absorber layer, the ETL has been chosen based on a matching conduction band offset with the absorber layer and the high electron mobility. Among the various options, TiO_2 offers minimum band offset and ease of synthesis. The front and back contacts are supposed to be ohmic and are made of silver (Ag) to maintain proper band alignment and reduce the band offset. It has been reported that tuning the CBM and VBM positions to keep a low band offset leads to superior device performance. Figure 6b exhibits the position of CBM/VBM in consecutive layers of the proposed structure. This further demonstrates the ease of charge transfers from the absorber to the respective transport layers.

The thickness and other simulation parameters for the active layer and the ETL were taken from the literature [17,50,51], while all the simulation parameters for Ge_2Se_2 have been derived from the DFT calculations as discussed in the previous section. All simulation parameters are summarized in Table 1

Performance estimation

Using the proposed model, we have estimated the performance of the solar cell in terms of open-circuit voltage (V_{oc}), short-circuit current density (J_{sc}), fill factor (FF), and power conversion efficiency (η). The performance of solar cells largely depends on various parameters, including the thickness of transport layers, absorber layers, and absolute temperature. Therefore, to get the optimum performance of the proposed device, we have optimized the performance of the cell module by varying the layer thicknesses of HTL, ETL, and absorber. Also, we have tested the performance of the device under the influence of varying defects densities in the active layer and the interfaces. The optimization corresponding to different parameters is summarized in the following sections.

Effect of HTL thickness variation

While the absorber layer is the crucial component of a solar cell, the role of the HTL cannot be overlooked because the choice of HTL plays a significant role in ensuring efficient charge transport, reducing recombination losses, and overall device stability. Therefore, numerous efforts have been made in

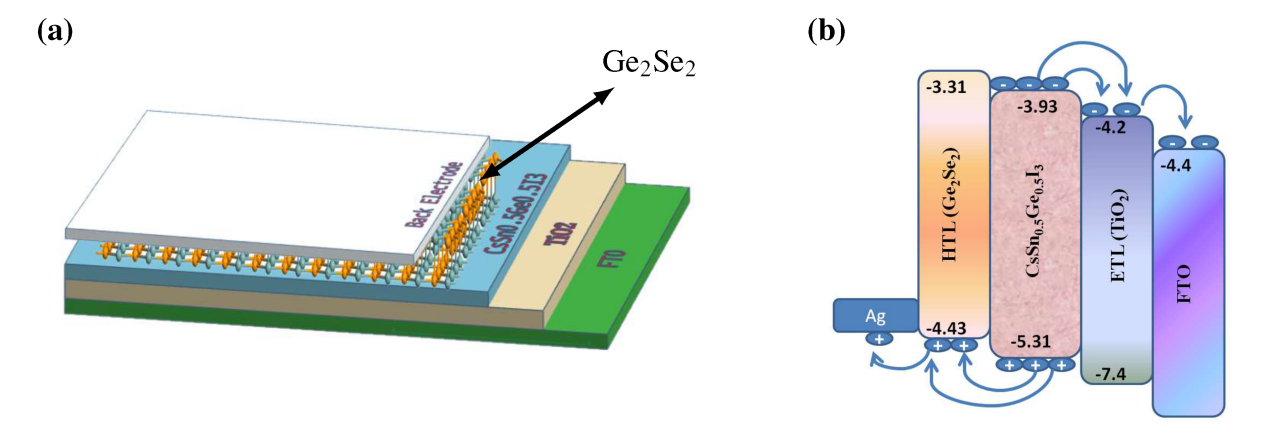

Figure 6: Schematic of the proposed PSC using Ge_2Se_2 as HTL; (a) device setup consisting of stacked layers of FTO–TiO_2–$CsSn_{0.5}Ge_{0.5}I_3$–Ge_2Se_2–Ag; (b) band offset among different PSC layers, demonstrating the ease of charge-transfer from the active layers to the respective transport layers.

Table 1: Simulation parameters for the proposed PSC.

Device parameter	FTO [50]	Ge_2Se_2 [our calculations]	$CsSn_{0.5}Ge_{0.5}I_3$ [51]	TiO_2 [17]
Bandgap (E_g) (eV)	3.4	1.12	1.5	3.26
Electron affinity (eV)	4.5	3.31	3.9	4.2
Dielectric constant (ε_r)	9.1	6.37	28	10
Conduction band effective DOS (cm^{-3})	1.1×10^{19}	0.1732×10^{19}	1.0×10^{19}	2.0×10^{17}
Valence band effective DOS (cm^{-3})	1.1×10^{19}	0.1887×10^{19}	1.0×10^{19}	6.0×10^{17}
Electron thermal velocity ($m \cdot s^{-1}$)	1×10^7	9.47×10^5	1×10^7	1×10^7
Hole thermal velocity ($m \cdot s^{-1}$)	1×10^7	2.66×10^5	1×10^7	1×10^7
Electron mobility ($cm^2 \cdot V^{-1} \cdot s^{-1}$)	20	300.451	974	100
Hole mobility ($cm^2 \cdot V^{-1} \cdot s^{-1}$)	10	187.003	213	25

the past to investigate suitable HTL materials for efficient solar cells [52-54]. The main function of the HTL is to capture the holes generated from the absorber layer and transfer them to the respective electrode. The thickness of the HTL also influences the device performance significantly. To optimize the HTL thickness for optimal device performance, we assumed a layer thickness of monolayer Ge_2Se_2, ranging from 1 to 10 nm. Figure 7a depicts the change of the performance parameters upon varying the HTL thickness.

It can be observed from Figure 7a that the device parameters decrease with higher HTL thickness. This behavior is mainly due to the appearance of a higher series resistance at larger HTL thicknesses. Also, a thick HTL may increase the chances of charge carrier recombination. Nevertheless, the performance degradation is very slight because of the ultrathin HTL layer proposed here. It is worth mentioning that there is an incremental rise in the short-circuit current density with thicker HTL. This is due to less carrier losses owing to reduced recombination at the interface of HTL and absorber layer and better surface cleavage because of the thick HTL [55,56]. Figure 7a indicates that 1 nm of HTL yields superior performance in terms of PCE, V_{oc}, J_{sc}, and FF with values of 28.148%, ≈1.11 V, 28.70 $mA \cdot cm^{-2}$, and ≈87.77% FF, respectively.

Effect of ETL thickness variation

In conjunction with the HTL, the ETL is responsible for collecting electrons generated in the active absorber layer. It is also necessary to optimize the ETL thickness to get an optimal device behavior. The change of the device parameters with varying ETL thickness is shown in Figure 7b. A higher thickness of the ETL leads to a worse device performance. When the layer thickness increases, the series resistance in the cell will also increase, and the light transmittance through the ETL decreases. The latter affects photogeneration in the perovskite layer, reducing J_{sc} and, consequently, the cell efficiency. Also, one can notice that the fill factor initially increases and then decreases mainly due to the small reverse saturation current for lower values of the ETL thickness. Later on, at higher ETL thicknesses, the fill factor decreases with increase in series resistance, and the cell efficiency decreases [57]. Since the ETL thickness is low, the impact on the performance degradation is insignificant. After examining all parameters, we found an optimized ETL thickness of 20 nm in our proposed device. The optimized values of the solar cell parameters at the optimal ETL thickness are 28.11%, ≈1.11 V, 28.68 $mA \cdot cm^{-2}$, and ≈87.81% for PCE, V_{oc}, J_{sc}, and FF, respectively.

Effect of absorber thickness variation

The absorber layer thickness is the most important and critical device parameter. The role of the absorber layer is to absorb the photons and generate charge carriers required for the current flow. It is intuitive to have a thick absorber layer for a higher current density. However, because the absorber thickness further affects the recombination rate, optimizing it for optimal device performance is necessary. The impact of varying absorber thickness on the different device parameters is summarized in Figure 7c. The absorber layer thickness was varied from 1 to 10 μm to obtain the optimal performance of the proposed device. Figure 7c shows that the short-circuit current density (J_{sc}) increases with higher absorber thickness up to a thickness of 4 μm, before reaching a constant value. The maximum short-circuit current density (J_{sc}) was calculated as 28.86 $mA \cdot cm^{-2}$ corresponding to an absorber thickness of 4 μm. The current variation followed the Beer–Lambert law, which justifies that more absorption will occur when the thickness of the absorber layer increases. A thicker absorber layer allows more photons to get absorbed, which leads to the generation of more electron–hole pairs. These generated electron–hole pairs, collected by the respective transport layers, contribute to the higher current density [58].

It is worth noticing that there is a significant impact of the absorber thickness on almost all parameters. The PCE increases

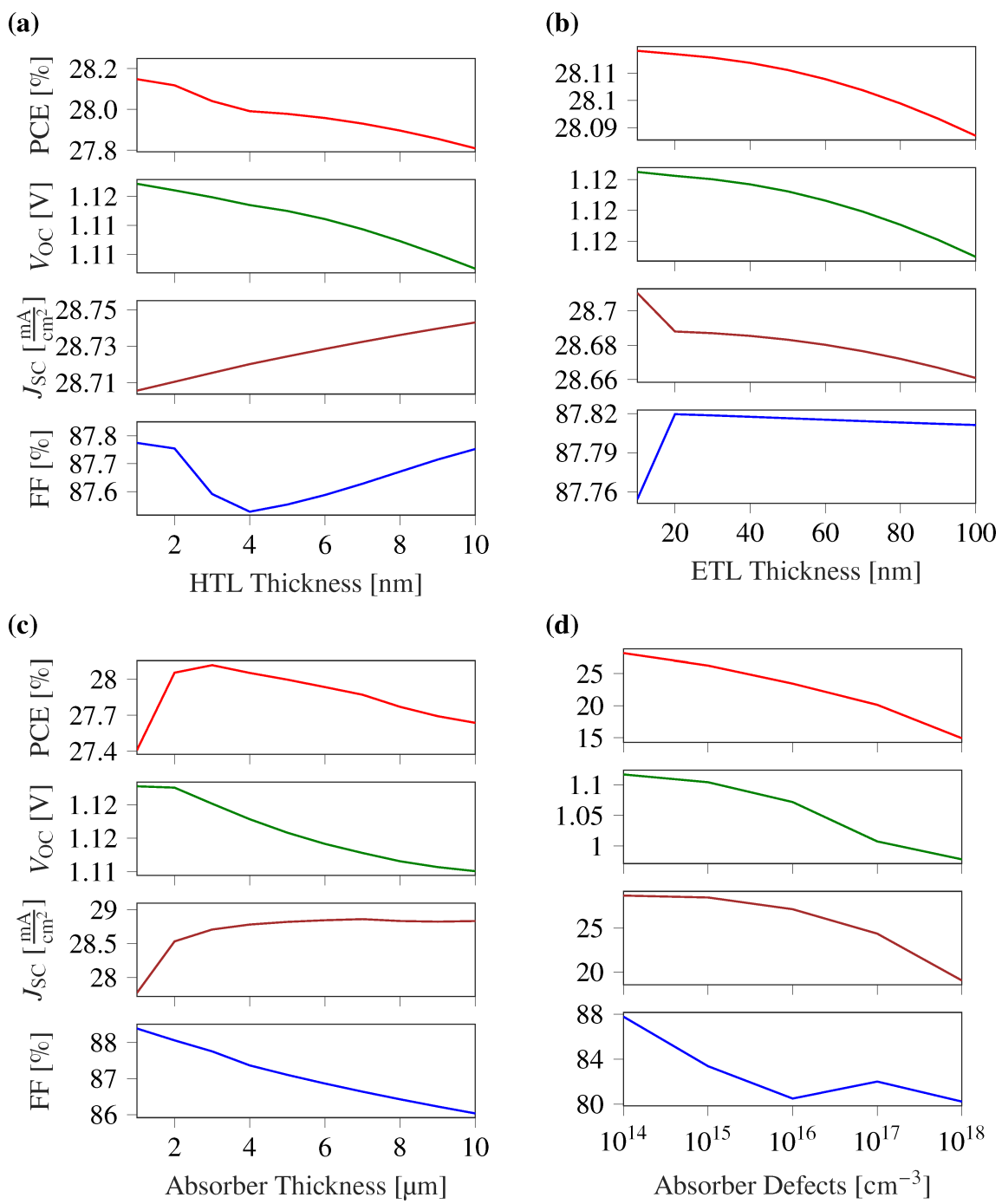

Figure 7: PSC performance parameters as functions of (a) HTL thickness, (b) ETL thickness, (c) absorber thickness, and (d) absorber defects. The device exhibits optimal performance at layer thicknesses of ETL, absorber, and HTL of 20 nm, 2 µm, and 1 nm, respectively.

from 27.4% to 28.11%, and the short-circuit current J_{sc} value reaches up to 28.86 mA·cm^{-2}. We observed that there is a significant reduction in FF and V_{oc} at higher absorber thicknesses, primarily because of the increasing series resistance and higher losses [59]. We set the optimal absorber thickness at 2 µm, above which the parameter variation was only very little.

Effect of defects in the absorber layer

Halide pervoskites are generally considered as defect-resilient; yet, deep level defects shows significant impact on the device performance [60,61]. Therefore, it is important to analyze their impact on the cell performance for better device design. Figure 7d shows the variation of the cell parameters at varying

absorber defect densities from 10^{14} cm^{-3} to 10^{18} cm^{-3}. Figure 7d shows that higher defect densities lead to worse device performance. This is due to the decrement in the lifetime of the charge carriers because of the shorter diffusion length, which results from the higher defect densities [62]. We can observed that the performance parameters decrease significantly above defect densities of 10^{15} cm^{-3}.

Effect of interface defects between active and transport layers

The photovoltaic behavior of halide perovskites is significantly affected by the properties of the interfaces. This is because a majority of defects arises at the junction between two layers during the fabrication of the device, caused by mismatches in the lattice structures, which lead to dangling bonds. These defects at the junctions play a critical role in the performance of the device as they contribute to increased local recombination at the interface. Within this particular PSC, two critical interface layers exist, namely, the interface between the absorber and the ETL and the interface between the absorber and the HTL. We analyzed the device performance by varying the defect densities at both interfaces within the range of 10^{6} cm^{-3} to 10^{15} cm^{-3}. Because of the ultrathin HTL layer, the absorber/HTL interface is more sensitive, and the device performance is anticipated to degrade above interface defect densities of 10^{7} cm^{-3}. However, the ETL/absorber interface exhibits excellent performance up to interface defects of 10^{12} cm^{-3} (Table 2), after which the device performance starts to deteriorate (Figure 8).

Table 2: Performance of the proposed PSC under 1.5G solar illumination.

Device parameter	Value
Open circuit voltage (V_{oc})	1.11 V
Short circuit current density (J_{sc})	28.70 mA·cm^{-2}
Fill factor (FF)	87.66%
Power conversion efficiency (PCE)	28.10%

The computed current density vs voltage curve is shown in Figure 9a, and the energy band diagram corresponding to the different layers is demonstrated in Figure 9b. We have also compared the proposed device with the combination of different transport layers in Table 3. It demonstrates that the proposed PSC structure excels in terms of performance parameters compared to other reported structures.

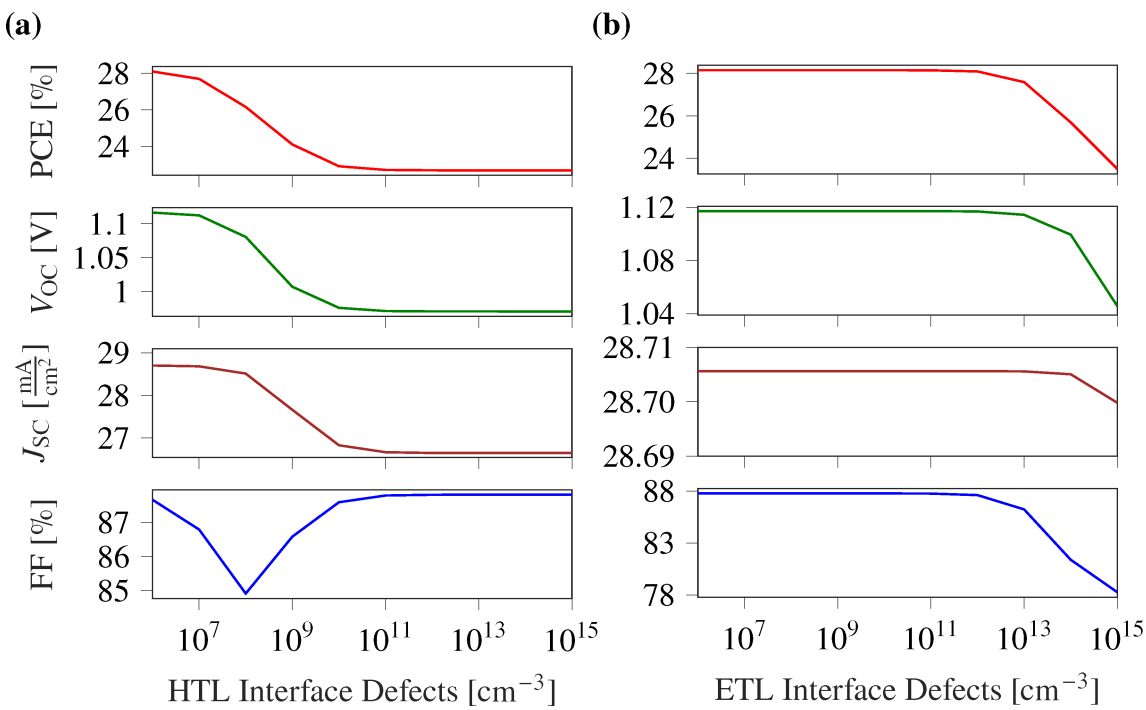

Figure 8: Variation of PSC performance parameters with interface defects between (a) ETL and active layer, and (b) active layer and HTL. Because of the ultrathin HTL layer, the interface at the absorber/HTL is more sensitive, and the device performance degrades for interface defect densities above 10^{7} cm^{-3}. However, the ETL/absorber interface exhibits an excellent performance up to the interface defects of 10^{12} cm^{-3}, after which the device performance starts to deteriorate.

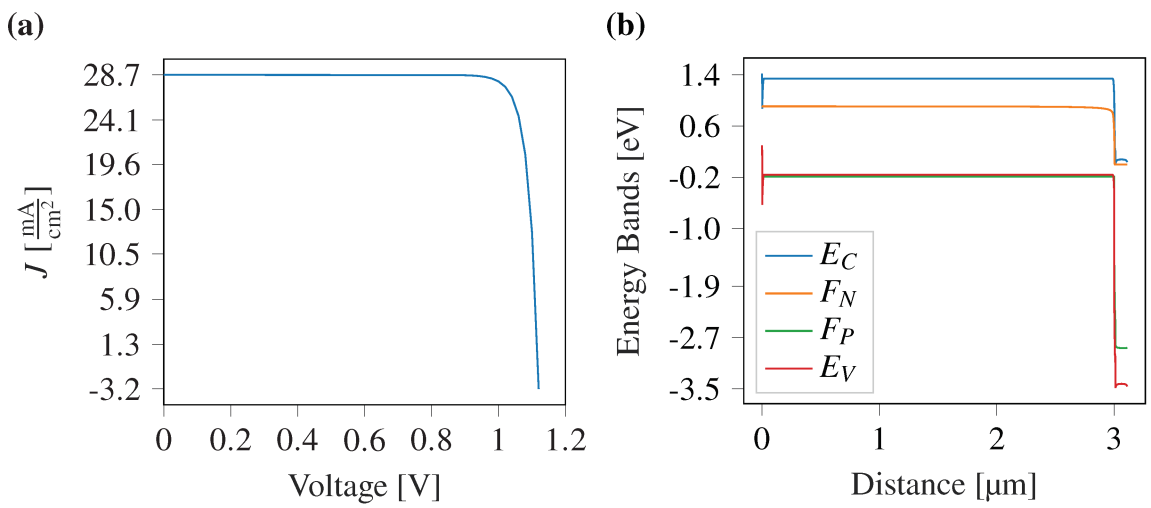

Figure 9: (a) Current density vs voltage curve for the proposed PSC, demonstrating a short-circuit current density and an open-circuit voltage of 28.7 mA·cm^{-2} and 1.11 V, respectively. (b) Energy band diagram for the proposed solar cell, where E_C stands for conduction band and E_V stands for valence band. F_N and F_P stand for quasi-Fermi levels of electrons and holes, respectively, at T = 300 K.

Table 3: Comparison of the PSC performance with earlier reported works.

Device configuration	V_{oc} (V)	J_{sc} (mA·cm^{-2})	FF (%)	PCE (%)
Ag/TiO_2/PSK/MoS_2/ITO [19]	0.93	26.24	83.0	29.43
Au/Cu_2O/PSK/TiO_2/FTO [63]	0.96	15.8	59.0	8.93
Au/MoS_2/PSK/WS_2/FTO [64]	0.96	27.3	87.62	22.17
Au/Spiro–OMeTAD/PSK/TiS_2/FTO [26]	0.95	20.05	66.90	12.75
Ag/Ge_2Se_2/PSK/TiO_2/FTO [This work]	1.11	28.70	87.66	28.10

Computational Methods

The methodology presented here (illustrated in Figure 10) is more generally valid and will apply to broader classes of 2D and 3D materials and structures. Therefore, we believe this section might serve as a mini tutorial for the computational design of future photovoltaic materials.

Material simulation using DFT

The structural and electronic properties have been investigated using an ab initio computational approach within the density functional theory (DFT) framework as implemented in the Quantum Espresso (QE) code [65,66].

We started our calculation to relax the structure at its most stable state (minimum energy) using the Broyden–Fletcher–Goldfarb–Shanno (BFGS) algorithm for a systematic computational study. It has been reported that the hybrid functional is more accurate in predicting the material behavior than local density approximation (LDA) [67] or generalized gradient approximation (GGA) [68] for modeling the exchange–correlation. Hence, for greater accuracy, we have used the Perdew–Burke–Ernzerhof (PBE) [69] and Heyd–Scuseria–Ernzerhof (HSE06) [70] functionals to model the exchange–correlation interactions with a screening parameter of 0.1 and mixing parameters of 25%. An ultrasoft, scalar relativistic pseudopotential of Troullier–Martins type [71] has been used to model the core corrections in the calculations. The valence electronic configuration for Ge and Se is taken as $4s^2 4p^2 3d^{10}$ and $4s^2 4p^4 3d^{10}$, respectively, and all electron-like wave functions have been generated using the projected augmented wave (PAW) method. A plane-wave basis set has been used to consolidate the interaction between core and valence electrons with an optimized threshold energy of 60 Ry. For efficient and precise calculations, the Brillouin zone has been sampled into 13 × 13 × 1 K-mesh points (using the Monkhorst–Pack scheme [72]) and high-energy/force convergence criteria of 10^{-10} eV/10^{-10} eV/Å^3, respectively, have been set for two consecutive self-consistent cycles. A sufficiently high vacuum of 23 Å is applied perpendicularly to avoid interlayer interactions.

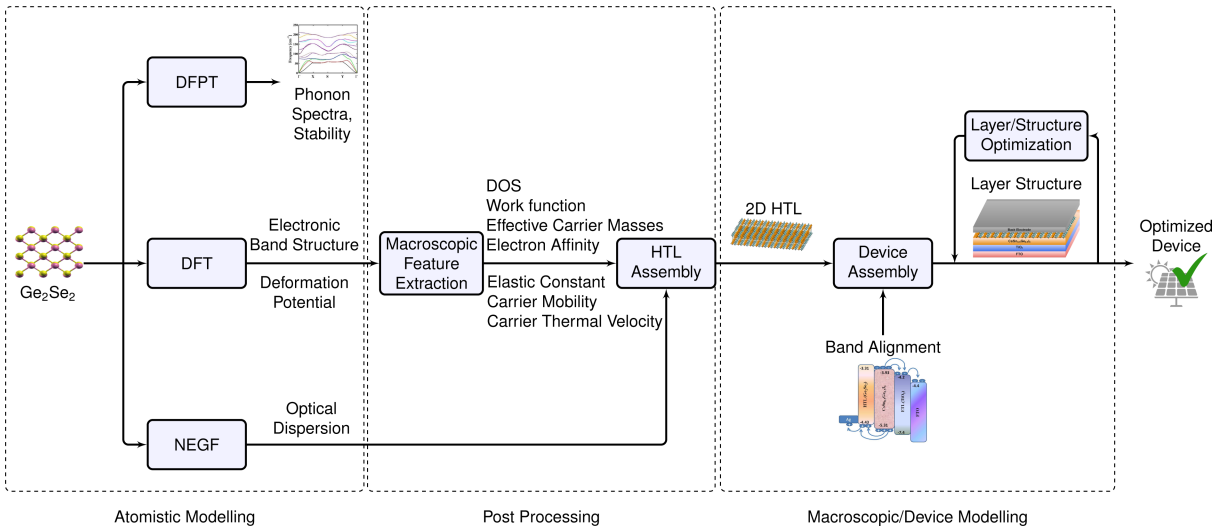

Figure 10: Computational pathway to estimate the materials' behavior and application in a PSC. First step – DFT geometry optimization, optimization of computational parameters, and electronic band structure and deformation potential extraction. Second step – test of the structural stability via density functional perturbation theory (DFPT): We compute the phonon spectra to verify the structure's dynamical stability. Third step – DFT-based electronic property estimation: We utilize the HSE functional to predict the band structure. Fourth step – DFT post-processing: (a) Extraction of the device-related parameters such as DOS, charge mobility, effective masses, thermal velocities, electron affinity, and work functions from fundamental physics equations together with DFT-post processing; (b) calculation of the optical behavior based on the non-equilibrium Green's function (NEGF) and the Kubo–Greenwood approaches. Fifth step – device design, simulation, and optimization: After proper band alignment and suitable material choices for the transport and active layers, we design a stacked solar cell, simulate it (in the SCAPS simulator), and optimize the individual layers for the best device performance.

The stability of the Ge_2Se_2 monolayer was estimated by phonon dispersion. The phonon dispersion has been calculated using density functional perturbation theory (DFPT), as implemented in the QE package. To compute the phonon spectra, we have estimated the second-order interatomic force constant using the relation [73]:

$$\Phi_{\alpha\beta} = \frac{\partial^2 \phi}{\partial r_\alpha \partial r_\beta}. \quad (1)$$

To maintain high accuracy, a large plane-wave mesh cutoff of 120 Ry is considered throughout the calculations.

Extraction of device-relevant parameters

To design a solar cell, we can derive some parameters from the DOS and E–k dispersion curves, such as the effective masses of electrons (m_e^*) and holes (m_h^*), the effective DOS in the conduction and valence bands (N_c and N_v), electron and hole thermal velocities (V_{th_e} and V_{th_h}), electron and hole mobilities, electron affinity, and work function. We outline an efficient approach to calculating these device parameters briefly below.

According to the K–P model, the charge carrier effective masses are given as $m^* = \frac{1}{\hbar^2}[\frac{\partial^2 E}{\partial k^2}]^{-1}$, where $\hbar$ is the reduced Plank constant, E is the charge carrier's energy, and k is a wave vector. To estimate the effective masses of electrons and holes, we used a curve-fitting algorithm (weighted least squares method) within a small parabolic section of the conduction band minima (CBM) and valence band maxima (VBM).

Using the charge carriers' effective masses, the effective DOS in the conduction and valence bands can be estimated as [74,75]:

$$N_c = 2\left[\frac{2\pi m_e^* k_B T}{\hbar^2}\right]^{3/2} \text{ and } N_v = 2\left[\frac{2\pi m_h^* k_B T}{\hbar^2}\right]^{3/2}, \quad (2)$$

where N_c and N_v are the effective DOS in the CB and VB, respectively, and the charge carriers' effective masses are m_e^* and m_h^* for electrons and holes, respectively. k_B, and T denote the Boltzmann constant and the absolute temperature, respectively.

We also calculated the electron and hole thermal velocities using their effective masses by [75,76]:

$$v_{th_e} = \sqrt{\frac{3k_B T}{m_e^*}} \text{ and } v_{th_h} = \sqrt{\frac{3k_B T}{m_h^*}}. \quad (3)$$

To compute the electron and hole mobilities, we have employed the deformation potential techniques [77] along with the acoustic phonon-limited approach. To estimate the phonon's limited mobility, we followed Bardeen–Shockley's approach [78], which says that the atomic displacement associated with a long wavelength acoustic phonon causes crystal deformation and significantly shifts the electronic energy dispersion. This change in the energy band edge with the differential displacement is characterized through the electron–phonon coupling Hamiltonian ($H_{\text{el-ph}}$) as:

$$H_{\text{el-ph}} = E_{\text{dp}} \nabla \cdot \vec{u}\left(\vec{r},t\right), \tag{4}$$

where E_{dp} is the deformation potential and $\vec{u}\left(\vec{r},t\right)$ is the displacement at the spatial coordinate $\vec{r}$ and time t. Further, van de Walle [79] suggested that the electron–phonon coupling Hamiltonian ($H_{\text{el-ph}}$) can be simplified to

$$\partial E\left(k\right) = E_{\text{dp}} \frac{\partial V}{V_0}, \tag{5}$$

where $\partial E(k)$ is the induced band edge shift due to the acoustic phonon and $\partial V/V_0$ is the fractional change in the unit cell volume due to the strain implication. After getting the value of the deformation potential using Kawaji theory [80], we can formulate the phonon-limited mobility ($\mu_{2\text{D}}$) because of the interaction of the charge carriers with low acoustic phonons as [81]:

$$\mu_{2\text{D}} = \frac{e\hbar^3 C}{k_{\text{B}} T m_{\text{e}}^* m_{\text{d}} E_{\text{dp}}^2}, \tag{6}$$

where C denotes the elastic constant of a 2D material and $m_d = \sqrt{m_x^* m_y^*}$ is the geometric mean of the effective masses. The elastic constant C can be derived by knowing the interatomic force constant, calculated applying a uniaxial strain δ in the direction of lattice vector a:

$$C = \frac{\partial^2 E}{\partial^2 \delta} \frac{1}{A_0}, \tag{7}$$

where A_0 is the surface area of the unit cell.The deformation potential E_{dp} can be calculated using a band edge variation formulation $E_{\text{dp}} = \partial E_{\text{edge}}/\partial\delta$, where E_{edge} is the valence and conduction band edge, and E_{dp} is computed by imposing a compressive and tensile strain δ to the unit cell. After substituting the values of E_{dp}, elastic constant C, and average effective mass m_{d}, we calculate the mobility of the charge carriers (for electrons and holes).

To calculate the charge transfer and use it in the solar cell, it is required to know the electron affinity and work function of monolayer Ge_2Se_2. The electron affinity is calculated as $E_{\text{A}} = E_{\text{Vac}} - E_{\text{LUMO}}$, where E_{A} is the electron affinity, E_{Vac} is the vacuum energy level, E_{LUMO} is the LUMO energy level. The ionization potential is calculated as IP = $E_{\text{Vac}} - E_{\text{HOMO}}$, where IP, E_{Vac}, and E_{HOMO} are ionization potential, vacuum energy level, and HOMO energy level, respectively. The electron affinity at a semiconductor surface is defined as the energy needed to carry an electron from the vacuum to the bottom of the conduction band. Similarly, the work function is defined as the minimum energy required by an electron of the material to escape into the vacuum [82,83]. E_{A} can be calculated using DFT as the energy difference between the vacuum level (E_{Vac}) and the Kohn–Sham (KS) eigenvalues relative to the bottom of the conduction band. Along with the DFT-derived parameters, some excited state eigenfunctions in terms of absorption coefficient and dielectric constant are also required to simulate solar cell-based devices. An optimum way of extracting these optical parameters from ground-state eigenvalues is described below.

Extraction of optical properties

To explore the optical properties, including dielectric constant, refractive index, absorption constant, extinction coefficient, and susceptibility for monolayer Ge_2Se_2, we employed the non-equilibrium Green's function (NEGF) and the Kubo–Greenwood formalisms [84] as described in the Synopsys-ATK [85]. A double zeta-polarized (DZDP) basis set has been used with a localized pseudo atomic orbital to calculate optical properties and characterize the valence electrons of the constituent atoms. To maintain high accuracy, a large plane-wave mesh cutoff of 120 Ry is considered throughout the calculations. We computed the optical parameters within the range of 0–30 eV. They stem from the dielectric function (using the Kramers–Kronig relations [86]), further estimated through the susceptibility tensors. The susceptibility tensors and complex dielectric functions are related as:

$$\chi_{ij}\left(\omega\right) = \frac{e^2}{\hbar m_{\text{e}}^2 V} \sum_{nm\mathbf{k}} \frac{f_{m\mathbf{k}} - f_{n\mathbf{k}}}{\omega_{nm}^2\left(\mathbf{k}\right)\left[\omega_{nm}\left(\mathbf{k}\right) - \omega - i\Gamma/\hbar\right]} p_{nm}^i\left(\mathbf{k}\right) p_{mn}^j\left(\mathbf{k}\right), \tag{8}$$

where $p_{nm}^i\left(\mathbf{k}\right) = \left\langle n\mathbf{k}\middle|\mathbf{p}^i\middle|m\mathbf{k}\right\rangle$ is the i-th component (labeling electrons) of the momentum operator between states n and m, m_{e} and e are the electron mass and charge, respectively, V is the

volume, Γ the energy broadening, and $\hbar\omega_{nm} = E_n - E_m$ and $f_{n\mathbf{k}}$ is the Fermi function (evaluated at the energy $E_n(\mathbf{k})$).

The response coefficients, that is, the relative dielectric permittivity (ε_r), the polarizability (α), and the optical conductivity (σ), are related to the susceptibility as:

$$\varepsilon_{r,ij}(\omega) = \left(1 + \chi_{ij}(\omega)\right), \tag{9}$$

$$\alpha_{ij}(\omega) = V\varepsilon_0\chi_{ij}(\omega), \tag{10}$$

$$\sigma_{ij}(\omega) = -i\omega\varepsilon_0\chi_{ij}(\omega), \tag{11}$$

with $i,j \in \{1,2,3\}$. Solving and separating Equation 9 for the imaginary part of dielectric function, we can calculate the refractive index and extinction coefficient as

$$\varepsilon_2(\omega) = \frac{2e^2\pi}{\Omega\varepsilon_0}\sum_{k,v,c}\left|\left\langle\Psi_k^c\left|\mathbf{u}\cdot\mathbf{r}\right|\Psi_k^v\right\rangle\right|^2\delta\left[E_k^c - E_k^v - E\right]. \tag{12}$$

Here, $\left|\Psi_k^c\right\rangle$ and $\left|\Psi_k^v\right\rangle$ are the conduction and valence band Bloch states with energies E_k^c and E_k^v, respectively, **r** is the position of the electron, and **u** is the polarization of light. e is the electronic charge, and **Ω** is the volume. Via the well-known relationship between relative permittivity and refractive index $n = \eta + i\kappa = \sqrt{\varepsilon_r}$, we finally get the following relationships for the refractive index and the absorption coefficient.

Refractive index/optical density:

$$\eta(\omega) = \left[\sqrt{\varepsilon_1^2(\omega) + \varepsilon_2^2(\omega)} + \frac{\varepsilon_2(\omega)}{2}\right]^{1/2} \tag{13}$$

Extinction coefficient:

$$\kappa(\omega) = \left[\sqrt{\varepsilon_1^2(\omega) + \varepsilon_2^2(\omega)} - \frac{\varepsilon_2(\omega)}{2}\right]^{1/2} \tag{14}$$

Absorption coefficient:

$$\alpha(\omega) = \sqrt{2\pi}\left[\sqrt{\varepsilon_1^2(\omega) + \varepsilon_2^2(\omega)} - \varepsilon_1(\omega)\right]^{1/2} \tag{15}$$

Device modeling

To investigate the performance of the proposed solar cell, we performed a numerical simulation using SCAPS-1D, which solves the fundamental semiconductor equations such as drift–diffusion, Poisson's equation, and continuity equations as:

$$\frac{\partial}{\partial x}\left(\varepsilon_0\varepsilon_r\frac{\partial\phi}{\partial x}\right) = -q\left(p - n + N_D^+ - N_A^- + \frac{\rho_{\text{def}}}{q}\right), \tag{16}$$

$$-\frac{\partial J_n}{\partial x} - U_n + G_n = \frac{\partial n}{\partial t}, \tag{17}$$

and

$$-\frac{\partial J_p}{\partial x} - U_n + G_n = \frac{\partial n}{\partial t}, \tag{18}$$

where $J_n = -\frac{\mu_n n}{q}\frac{\partial E_{\text{F}n}}{\partial x}$ and $J_p = -\frac{\mu_p p}{q}\frac{\partial E_{\text{F}p}}{\partial x}$ are the electron and hole current densities at the Fermi levels $E_{\text{F}n}$ and $E_{\text{F}p}$, respectively. ε_0, ε_r, ϕ, q, n, and p denote the absolute and relative permittivity, the electrostatic potential, the electronic charge, and the electron and hole concentrations, respectively. The charge carrier mobilities, generation, and recombination rates for electrons and holes are represented by μ_n, G_n, U_n, μ_p, G_p, U_p, respectively. All these parameters are functions of the position coordinate x.

During the simulation of the proposed device, it is assumed that the reflection of the top surface is zero. In contrast, the reflection from the back surface is considered as 100%, so the all incident photons have greater energy than the bandgap of the materials and can contribute to generating charge carriers. The generated charge carrier mobility of the chosen material assists in delivering it up to the contacts.

Conclusion

This contribution investigates the electronic and optical properties of monolayer Ge_2Se_2 using DFT. The structure of the monolayer is properly optimized and relaxed for its lowest energy state. Tough threshold criteria have been chosen to maintain high precision in the calculation, along with a hybrid functional for modeling the exchange–correlation interactions. The non-imaginary frequencies in the phonon spectra confirm the stable geometry of the investigated structure. The electronic properties of the monolayer have been investigated in detail in terms of energy band diagram, effective masses of the charge carriers, mobility of electrons and holes at room temperature,

the total density of states along with effective densities in conduction and valence band, electron affinity, and ionization potentials. In addition, the optical behavior of monolayer Ge_2Se_2 has been discussed through exhaustive calculations of the material's absorption coefficient, dielectric constants, refractive index, and extinction coefficient. The optimum bandgap (1.2 eV), high carrier mobility, and promising optical characteristics of monolayer Ge_2Se_2 further led us to investigate the application of the investigated structure. To show the application of monolayer Ge_2Se_2, a perovskite solar cell has been proposed using monolayer Ge_2Se_2 as HTL. The optimal performance was determined under AM1.5G spectrum illumination. To obtain the optimum device performance, first, the ETL thickness has been varied from 10 to 100 nm, where it is found that above 20 nm, the device performance starts to diminish. Further keeping the ETL thickness at 20 nm, the absorber thickness has been tuned from 1 to 10 µm. The simulation results show an optimal device performance at 2 µm absorber thickness. Keeping the thickness of ETL and absorber layer at 20 nm and 2 µm, respectively, the HTL thickness has been changed from 1 to 10 nm. As the thickness increases, the device performance diminishes because of recombination of charge carriers in the HTL. Thus, the device exhibits optimal performance at layer thicknesses of ETL, absorber, and HTL at 20 nm, 2 µm, and 1 nm, respectively. The simulation results indicate that the proposed solar cell outperforms in terms of power conversion efficiency (around 28%) and fill factor (≈87%). In addition to the proposed solar cell, the excellent optoelectronic characteristics of the investigated monolayer Ge_2Se_2 make it a potential candidate for other photo devices. This study may also be helpful in the search for excelling materials regarding prospective applications in photo devices.

Acknowledgements

The authors would like to thank Dr. Marc Burgelman and his team from Gent University for providing the SCAPS simulator.

Funding

Anup Shrivastava acknowledges the Ministry of Education (Govt. of India) for providing financial support. Sanjai Singh acknowledges the Centralised Computation Facility, IIIT-Allahabad, for providing computational resources.

Author Contributions

Anup Shrivastava: conceptualization; formal analysis; investigation; methodology; writing – original draft. Shivani Saini: methodology; software; writing – original draft. Dolly Kumari: methodology; software. Sanjai Singh: resources; supervision; writing – review & editing. Jost Adam: project administration; supervision; validation; visualization; writing – review & editing.

ORCID® iDs

Anup Shrivastava - https://orcid.org/0000-0003-1601-5947
Shivani Saini - https://orcid.org/0000-0003-2290-8872
Dolly Kumari - https://orcid.org/0000-0003-4823-4802
Sanjai Singh - https://orcid.org/0000-0002-1783-8729
Jost Adam - https://orcid.org/0000-0001-7177-3252

Data Availability Statement

All data that supports the findings of this study is available in the published article and/or the supporting information to this article.

References

1. Noel, N. K.; Stranks, S. D.; Abate, A.; Wehrenfennig, C.; Guarnera, S.; Haghighirad, A.-A.; Sadhanala, A.; Eperon, G. E.; Pathak, S. K.; Johnston, M. B.; Petrozza, A.; Herz, L. M.; Snaith, H. J. *Energy Environ. Sci.* **2014,** *7,* 3061–3068. doi:10.1039/c4ee01076k
2. Miah, M. H.; Khandaker, M. U.; Rahman, M. B.; Nur-E-Alam, M.; Islam, M. A. *RSC Adv.* **2024,** *14,* 15876–15906. doi:10.1039/d4ra01640h
3. Salhi, B.; Wudil, Y. S.; Hossain, M. K.; Al-Ahmed, A.; Al-Sulaiman, F. A. *Renewable Sustainable Energy Rev.* **2018,** *90,* 210–222. doi:10.1016/j.rser.2018.03.058
4. Helal Miah, M.; Bulu Rahman, M.; Khatun, F.; Khandaker, M. U.; Wan Muhammad Hatta, S. F.; Soin, N. B.; Islam, M. A. *Optik (Munich, Ger.)* **2023,** *281,* 170819. doi:10.1016/j.ijleo.2023.170819
5. Kumar, V.; Kathiravan, A.; Jhonsi, M. A. *Nano Energy* **2024,** *125,* 109523. doi:10.1016/j.nanoen.2024.109523
6. Berhe, T. A.; Su, W.-N.; Chen, C.-H.; Pan, C.-J.; Cheng, J.-H.; Chen, H.-M.; Tsai, M.-C.; Chen, L.-Y.; Dubale, A. A.; Hwang, B.-J. *Energy Environ. Sci.* **2016,** *9,* 323–356. doi:10.1039/c5ee02733k
7. Di Carlo, A.; Agresti, A.; Brunetti, F.; Pescetelli, S. *JPhys Energy* **2020,** *2,* 031003. doi:10.1088/2515-7655/ab9eab
8. Miao, S.; Liu, T.; Du, Y.; Zhou, X.; Gao, J.; Xie, Y.; Shen, F.; Liu, Y.; Cho, Y. *Nanomaterials* **2022,** *12,* 2100. doi:10.3390/nano12122100
9. Zhang, H. *ACS Nano* **2015,** *9,* 9451–9469. doi:10.1021/acsnano.5b05040
10. Kumar, S.; Taunk, M. *Mater. Today Phys.* **2024,** *46,* 101483. doi:10.1016/j.mtphys.2024.101483
11. Gupta, A.; Sakthivel, T.; Seal, S. *Prog. Mater. Sci.* **2015,** *73,* 44–126. doi:10.1016/j.pmatsci.2015.02.002
12. Zhou, D.; Zhou, T.; Tian, Y.; Zhu, X.; Tu, Y. *J. Nanomater.* **2018,** *2018,* 8148072. doi:10.1155/2018/8148072
13. Ciambelli, P.; La Guardia, G.; Vitale, L. Nanotechnology for green materials and processes. In *Studies in Surface Science and Catalysis;* Basile, A.; Centi, G.; Falco, M. D.; Iaquaniello, G., Eds.; Elsevier: Amsterdam, Netherlands, 2020; Vol. 179, pp 97–116. doi:10.1016/b978-0-444-64337-7.00007-0
14. Shao, S.; Loi, M. A. *Adv. Mater. Interfaces* **2020,** *7,* 1901469. doi:10.1002/admi.201901469
15. Zhang, L.; Liu, T.; Liu, L.; Hu, M.; Yang, Y.; Mei, A.; Han, H. *J. Mater. Chem. A* **2015,** *3,* 9165–9170. doi:10.1039/c4ta04647a
16. Wang, K.-C.; Jeng, J.-Y.; Shen, P.-S.; Chang, Y.-C.; Diau, E. W.-G.; Tsai, C.-H.; Chao, T.-Y.; Hsu, H.-C.; Lin, P.-Y.; Chen, P.; Guo, T.-F.; Wen, T.-C. *Sci. Rep.* **2014,** *4,* 4756. doi:10.1038/srep04756
17. Hima, A.; Lakhdar, N. *Opt. Mater. (Amsterdam, Neth.)* **2020,** *99,* 109607. doi:10.1016/j.optmat.2019.109607

18. Kukreti, S.; Gupta, G. K.; Dixit, A. *Sol. Energy* **2021,** *225,* 802–813. doi:10.1016/j.solener.2021.07.071
19. Kohnehpoushi, S.; Nazari, P.; Nejand, B. A.; Eskandari, M. *Nanotechnology* **2018,** *29,* 205201. doi:10.1088/1361-6528/aab1d4
20. Kumar Singh, M.; V. Shinde, P.; Singh, P.; Kumar Tyagi, P. Two-Dimensional Materials for Advanced Solar Cells. In *Solar Cells - Theory, Materials and Recent Advances;* Elseman, A., Ed.; IntechOpen: London, United Kingdom, 2021. doi:10.5772/intechopen.94114
21. Bati, A. S. R.; Batmunkh, M.; Shapter, J. G. *Adv. Energy Mater.* **2020,** *10,* 1902253. doi:10.1002/aenm.201902253
22. Ross, J. S.; Klement, P.; Jones, A. M.; Ghimire, N. J.; Yan, J.; Mandrus, D. G.; Taniguchi, T.; Watanabe, K.; Kitamura, K.; Yao, W.; Cobden, D. H.; Xu, X. *Nat. Nanotechnol.* **2014,** *9,* 268–272. doi:10.1038/nnano.2014.26
23. Wang, Q. H.; Kalantar-Zadeh, K.; Kis, A.; Coleman, J. N.; Strano, M. S. *Nat. Nanotechnol.* **2012,** *7,* 699–712. doi:10.1038/nnano.2012.193
24. Li, H.; Shi, Y.; Chiu, M.-H.; Li, L.-J. *Nano Energy* **2015,** *18,* 293–305. doi:10.1016/j.nanoen.2015.10.023
25. Bernardi, M.; Palummo, M.; Grossman, J. C. *Nano Lett.* **2013,** *13,* 3664–3670. doi:10.1021/nl401544y
26. Yin, G.; Zhao, H.; Feng, J.; Sun, J.; Yan, J.; Liu, Z.; Lin, S.; Liu, S. F. *J. Mater. Chem. A* **2018,** *6,* 9132–9138. doi:10.1039/c8ta01143e
27. Zhao, X.; Liu, S.; Zhang, H.; Chang, S.-Y.; Huang, W.; Zhu, B.; Shen, Y.; Shen, C.; Wang, D.; Yang, Y.; Wang, M. *Adv. Funct. Mater.* **2019,** *29,* 1805168. doi:10.1002/adfm.201805168
28. Mukherjee, B.; Cai, Y.; Tan, H. R.; Feng, Y. P.; Tok, E. S.; Sow, C. H. *ACS Appl. Mater. Interfaces* **2013,** *5,* 9594–9604. doi:10.1021/am402550s
29. Chang, K.; Parkin, S. S. P. *APL Mater.* **2019,** *7,* 041102. doi:10.1063/1.5091546
30. An, B.; Ma, Y.; Zhang, G.; You, C.; Zhang, Y. *RSC Adv.* **2020,** *10,* 42157–42163. doi:10.1039/d0ra08360g
31. Lin, Y.-T.; Shi, J.-B.; Chen, Y.-C.; Chen, C.-J.; Wu, P.-F. *Nanoscale Res. Lett.* **2009,** *4,* 694–698. doi:10.1007/s11671-009-9299-5
32. Zhou, X.; Zhang, Q.; Gan, L.; Li, H.; Xiong, J.; Zhai, T. *Adv. Sci.* **2016,** *3,* 1600177. doi:10.1002/advs.201600177
33. Xia, J.; Li, X.-Z.; Huang, X.; Mao, N.; Zhu, D.-D.; Wang, L.; Xu, H.; Meng, X.-M. *Nanoscale* **2016,** *8,* 2063–2070. doi:10.1039/c5nr07675g
34. Huang, Y.; Ling, C.; Liu, H.; Wang, S.; Geng, B. *J. Phys. Chem. C* **2014,** *118,* 9251–9260. doi:10.1021/jp5013158
35. Wang, X.; Liu, B.; Wang, Q.; Song, W.; Hou, X.; Chen, D.; Cheng, Y.-b.; Shen, G. *Adv. Mater. (Weinheim, Ger.)* **2013,** *25,* 1479–1486. doi:10.1002/adma.201204063
36. Mukherjee, B.; Tok, E. S.; Sow, C. H. *J. Appl. Phys.* **2013,** *114,* 134302. doi:10.1063/1.4823779
37. Mukherjee, B.; Hu, Z.; Zheng, M.; Cai, Y.; Feng, Y. P.; Tok, E. S.; Sow, C. H. *J. Mater. Chem.* **2012,** *22,* 24882–24888. doi:10.1039/c2jm35006h
38. Properzi, L.; Di Cicco, A.; Nataf, L.; Baudelet, F.; Irifune, T. *Sci. Rep.* **2015,** *5,* 10188. doi:10.1038/srep10188
39. Zang, H.; Routh, P. K.; Huang, Y.; Chen, J.-S.; Sutter, E.; Sutter, P.; Cotlet, M. *ACS Nano* **2016,** *10,* 4790–4796. doi:10.1021/acsnano.6b01538
40. Zhou, T.; Pang, W. K.; Zhang, C.; Yang, J.; Chen, Z.; Liu, H. K.; Guo, Z. *ACS Nano* **2014,** *8,* 8323–8333. doi:10.1021/nn503582c
41. Saini, S.; Shrivastava, A.; Singh, S. *Phys. E (Amsterdam, Neth.)* **2022,** *138,* 115060. doi:10.1016/j.physe.2021.115060
42. Seixas, L. *J. Appl. Phys.* **2020,** *128,* 045115. doi:10.1063/5.0012427
43. Kong, B. D.; Paul, S.; Nardelli, M. B.; Kim, K. W. *Phys. Rev. B: Condens. Matter Mater. Phys.* **2009,** *80,* 033406. doi:10.1103/physrevb.80.033406
44. Qin, G.; Yan, Q.-B.; Qin, Z.; Yue, S.-Y.; Hu, M.; Su, G. *Phys. Chem. Chem. Phys.* **2015,** *17,* 4854–4858. doi:10.1039/c4cp04858j
45. Peng, B.; Zhang, H.; Shao, H.; Xu, Y.; Zhang, X.; Zhu, H. *Sci. Rep.* **2016,** *6,* 20225. doi:10.1038/srep20225
46. Haastrup, S.; Strange, M.; Pandey, M.; Deilmann, T.; Schmidt, P. S.; Hinsche, N. F.; Gjerding, M. N.; Torelli, D.; Larsen, P. M.; Riis-Jensen, A. C.; Gath, J.; Jacobsen, K. W.; Jørgen Mortensen, J.; Olsen, T.; Thygesen, K. S. *2D Mater.* **2018,** *5,* 042002. doi:10.1088/2053-1583/aacfc1
47. Gjerding, M. N.; Taghizadeh, A.; Rasmussen, A.; Ali, S.; Bertoldo, F.; Deilmann, T.; Knøsgaard, N. R.; Kruse, M.; Larsen, A. H.; Manti, S.; Pedersen, T. G.; Petralanda, U.; Skovhus, T.; Svendsen, M. K.; Mortensen, J. J.; Olsen, T.; Thygesen, K. S. *2D Mater.* **2021,** *8,* 044002. doi:10.1088/2053-1583/ac1059
48. Chattopadhyay, S.; Kokenyesi, R. S.; Hong, M. J.; Watts, C. L.; Labram, J. G. *J. Mater. Chem. C* **2020,** *8,* 10761–10766. doi:10.1039/d0tc00328j
49. Kahn, A. *Mater. Horiz.* **2016,** *3,* 7–10. doi:10.1039/c5mh00160a
50. Singh, D.; Gupta, S. K.; Sonvane, Y.; Lukačević, I. *J. Mater. Chem. C* **2016,** *4,* 6386–6390. doi:10.1039/c6tc01913g
51. Patel, P. K. *Sci. Rep.* **2021,** *11,* 3082. doi:10.1038/s41598-021-82817-w
52. Urieta-Mora, J.; García-Benito, I.; Molina-Ontoria, A.; Martín, N. *Chem. Soc. Rev.* **2018,** *47,* 8541–8571. doi:10.1039/c8cs00262b
53. Kim, G.-W.; Choi, H.; Kim, M.; Lee, J.; Son, S. Y.; Park, T. *Adv. Energy Mater.* **2020,** *10,* 1903403. doi:10.1002/aenm.201903403
54. Wang, D.; Elumalai, N. K.; Mahmud, M. A.; Yi, H.; Upama, M. B.; Lee Chin, R. A.; Conibeer, G.; Xu, C.; Haque, F.; Duan, L.; Uddin, A. *Synth. Met.* **2018,** *246,* 195–203. doi:10.1016/j.synthmet.2018.10.012
55. Bag, A.; Radhakrishnan, R.; Nekovei, R.; Jeyakumar, R. *Sol. Energy* **2020,** *196,* 177–182. doi:10.1016/j.solener.2019.12.014
56. Kim, G.-W.; Shinde, D. V.; Park, T. *RSC Adv.* **2015,** *5,* 99356–99360. doi:10.1039/c5ra18648j
57. Jeyakumar, R.; Bag, A.; Nekovei, R.; Radhakrishnan, R. *J. Electron. Mater.* **2020,** *49,* 3533–3539. doi:10.1007/s11664-020-08041-w
58. Kumari, D.; Pandey, S. K. *J. Opt. Soc. Am. B* **2022,** *39,* 756–763. doi:10.1364/josab.443938
59. Abdelaziz, W.; Shaker, A.; Abouelatta, M.; Zekry, A. *Opt. Mater. (Amsterdam, Neth.)* **2019,** *91,* 239–245. doi:10.1016/j.optmat.2019.03.023
60. Bhatt, S.; Shukla, R.; Pathak, C.; Pandey, S. K. *IEEE Trans. Electron Devices* **2020,** *67,* 2837–2843. doi:10.1109/ted.2020.2996570
61. Zhang, X.; Turiansky, M. E.; Van de Walle, C. G. *J. Phys. Chem. C* **2020,** *124,* 6022–6027. doi:10.1021/acs.jpcc.0c01324
62. Ahmed, S.; Jannat, F.; Khan, M. A. K.; Alim, M. A. *Optik (Munich, Ger.)* **2021,** *225,* 165765. doi:10.1016/j.ijleo.2020.165765
63. Nejand, B. A.; Ahmadi, V.; Gharibzadeh, S.; Shahverdi, H. R. *ChemSusChem* **2016,** *9,* 302–313. doi:10.1002/cssc.201501273
64. Kaity, A.; Shubham; Singh, S.; Pandey, S. K. *Superlattices Microstruct.* **2021,** *156,* 106972. doi:10.1016/j.spmi.2021.106972

65. Giannozzi, P.; Andreussi, O.; Brumme, T.; Bunau, O.; Buongiorno Nardelli, M.; Calandra, M.; Car, R.; Cavazzoni, C.; Ceresoli, D.; Cococcioni, M.; Colonna, N.; Carnimeo, I.; Dal Corso, A.; de Gironcoli, S.; Delugas, P.; DiStasio, R. A., Jr.; Ferretti, A.; Floris, A.; Fratesi, G.; Fugallo, G.; Gebauer, R.; Gerstmann, U.; Giustino, F.; Gorni, T.; Jia, J.; Kawamura, M.; Ko, H.-Y.; Kokalj, A.; Küçükbenli, E.; Lazzeri, M.; Marsili, M.; Marzari, N.; Mauri, F.; Nguyen, N. L.; Nguyen, H.-V.; Otero-de-la-Roza, A.; Paulatto, L.; Poncé, S.; Rocca, D.; Sabatini, R.; Santra, B.; Schlipf, M.; Seitsonen, A. P.; Smogunov, A.; Timrov, I.; Thonhauser, T.; Umari, P.; Vast, N.; Wu, X.; Baroni, S. *J. Phys.: Condens. Matter* **2017,** *29,* 465901. doi:10.1088/1361-648x/aa8f79
66. Giannozzi, P.; Baroni, S.; Bonini, N.; Calandra, M.; Car, R.; Cavazzoni, C.; Ceresoli, D.; Chiarotti, G. L.; Cococcioni, M.; Dabo, I.; Dal Corso, A.; de Gironcoli, S.; Fabris, S.; Fratesi, G.; Gebauer, R.; Gerstmann, U.; Gougoussis, C.; Kokalj, A.; Lazzeri, M.; Martin-Samos, L.; Marzari, N.; Mauri, F.; Mazzarello, R.; Paolini, S.; Pasquarello, A.; Paulatto, L.; Sbraccia, C.; Scandolo, S.; Sclauzero, G.; Seitsonen, A. P.; Smogunov, A.; Umari, P.; Wentzcovitch, R. M. *J. Phys.: Condens. Matter* **2009,** *21,* 395502. doi:10.1088/0953-8984/21/39/395502
67. Zhao, G. L.; Bagayoko, D.; Williams, T. D. *Phys. Rev. B: Condens. Matter Mater. Phys.* **1999,** *60,* 1563–1572. doi:10.1103/physrevb.60.1563
68. Grimme, S. *J. Comput. Chem.* **2006,** *27,* 1787–1799. doi:10.1002/jcc.20495
69. Perdew, J. P.; Burke, K.; Ernzerhof, M. *Phys. Rev. Lett.* **1996,** *77,* 3865–3868. doi:10.1103/physrevlett.77.3865
70. Heyd, J.; Scuseria, G. E.; Ernzerhof, M. *J. Chem. Phys.* **2003,** *118,* 8207–8215. doi:10.1063/1.1564060
71. Troullier, N.; Martins, J. L. *Phys. Rev. B: Condens. Matter Mater. Phys.* **1991,** *43,* 1993–2006. doi:10.1103/physrevb.43.1993
72. Monkhorst, H. J.; Pack, J. D. *Phys. Rev. B: Condens. Matter Mater. Phys.* **1976,** *13,* 5188–5192. doi:10.1103/physrevb.13.5188
73. Tadano, T.; Gohda, Y.; Tsuneyuki, S. *J. Phys.: Condens. Matter* **2014,** *26,* 225402. doi:10.1088/0953-8984/26/22/225402
74. Green, M. A. *J. Appl. Phys.* **1990,** *67,* 2944–2954. doi:10.1063/1.345414
75. Chaurasiya, R.; Gupta, G. K.; Dixit, A. *Sol. Energy Mater. Sol. Cells* **2019,** *201,* 110076. doi:10.1016/j.solmat.2019.110076
76. Cozza, D.; Ruiz, C. M.; Duche, D.; Simon, J. J.; Escoubas, L. *IEEE J. Photovoltaics* **2016,** *6,* 1292–1297. doi:10.1109/jphotov.2016.2576678
77. Shuai, Z.; Wang, L.; Song, C. *Deformation Potential Theory;* SpringerBriefs in Molecular Science; Springer Berlin: Berlin, Germany, 2012; pp 67–88. doi:10.1007/978-3-642-25076-7_4
78. Bardeen, J.; Shockley, W. *Phys. Rev.* **1950,** *80,* 72–80. doi:10.1103/physrev.80.72
79. Van de Walle, C. G. *Phys. Rev. B: Condens. Matter Mater. Phys.* **1989,** *39,* 1871–1883. doi:10.1103/physrevb.39.1871
80. Kawaji, S. *J. Phys. Soc. Jpn.* **1969,** *27,* 906–908. doi:10.1143/jpsj.27.906
81. Sharma, G.; Datta, S.; Ghosh, P. *J. Electron. Mater.* **2021,** *50,* 1644–1654. doi:10.1007/s11664-020-08479-y
82. Khan, F.; Din, H. U.; Khan, S. A.; Rehman, G.; Bilal, M.; Nguyen, C. V.; Ahmad, I.; Gan, L.-Y.; Amin, B. *J. Phys. Chem. Solids* **2019,** *126,* 304–309. doi:10.1016/j.jpcs.2018.11.021
83. Madas, S.; Mishra, S. K.; Kahaly, S.; Kahaly, M. U. *Sci. Rep.* **2019,** *9,* 10307. doi:10.1038/s41598-019-44823-x
84. Sipe, J. E.; Ghahramani, E. *Phys. Rev. B: Condens. Matter Mater. Phys.* **1993,** *48,* 11705–11722. doi:10.1103/physrevb.48.11705
85. Smidstrup, S.; Markussen, T.; Vancraeyveld, P.; Wellendorff, J.; Schneider, J.; Gunst, T.; Verstichel, B.; Stradi, D.; Khomyakov, P. A.; Vej-Hansen, U. G.; Lee, M.-E.; Chill, S. T.; Rasmussen, F.; Penazzi, G.; Corsetti, F.; Ojanperä, A.; Jensen, K.; Palsgaard, M. L. N.; Martinez, U.; Blom, A.; Brandbyge, M.; Stokbro, K. *J. Phys.: Condens. Matter* **2020,** *32,* 015901. doi:10.1088/1361-648x/ab4007
86. Probert, M. *Contemp. Phys.* **2020,** *61,* 312. doi:10.1080/00107514.2021.1890832

License and Terms

This is an open access article licensed under the terms of the Beilstein-Institut Open Access License Agreement (https://www.beilstein-journals.org/bjnano/terms), which is identical to the Creative Commons Attribution 4.0 International License (https://creativecommons.org/licenses/by/4.0). The reuse of material under this license requires that the author(s), source and license are credited. Third-party material in this article could be subject to other licenses (typically indicated in the credit line), and in this case, users are required to obtain permission from the license holder to reuse the material.

The definitive version of this article is the electronic one which can be found at:
https://doi.org/10.3762/bjnano.15.94